Electronic Supplementary Material (ESI) for Inorganic Chemistry Frontiers.

Supporting Information for

Regulation on the electronic structure and surface wettability of Co_9S_8 electrocatalyst by nitrogen and phosphorous co-doping for efficient overall water splitting

Chunyan Xiang,[a] Dahai Zeng,[a,*] Bing Du,[b] Xiaoxi Huang,[c] Huaijun Lin,[a] Peng Zhang,[a] Zhiguo Zhang,[a] Dexin Chen,[a] Wei Li,[a] Yuying Meng [a,*]

[a] Institute of Advanced Wear and Corrosion Resistant and Functional Materials, Jinan University, 601 Huangpu Avenue West, Guangzhou, 510632, China

[b] College of Materials Science and Engineering, Shenzhen University, 1066 Xueyuan Avenue, Shenzhen, 518060, China

[c] Hoffmann Institute of Advanced Materials, Postdoctoral Innovation Practice Base, Shenzhen Polytechnic, 7098 Liuxian Blvd, Shenzhen, Nanshan District, 518055, China

* Corresponding Authors: Y. Meng (yymeng9169@jnu.edu.cn)

D. Zeng (dahyzeng@jnu.edu.cn)

Additional Experimental

1. Chemicals and reagents

Cobalt foam (CF, thickness: 1.6 mm, bulk density: 0.8 g/cm^3) was purchased from Kunshan Lvchuang Electronic Technology Co., Ltd. Thiourea ($CS(NH_2)_2$, 99%) was acquired from Aladdin. Potassium hydroxide (KOH, 85%), drochloric acid (HCl, 36~38wt.%), sulfuric acid (H_2SO_4, 98%), acetone (99.5%) and absolute ethanol were obtained from Guangzhou Chemical Reagent Factory. Diammonium hydrogen phosphate ($(NH_4)_2HPO_4$, 99%) and sodium hypophosphite ($NaH_2PO_2 \cdot H_2O$, 99%) were obtained from Tianjin Damao Chemical Reagent Factory and Tianjin Yongda Chemical Reagent Co., Ltd, respectively. Pt/C (20 wt.%) and Nafion (5 wt.%) were purchased from Sigma-Aldrich. All the chemicals were of analytical grade and used as received without any treatment. Deionized water (resistance > 18 M cm) was employed throughout the experiments.

2. Preparation of N,P-Co_9S_8

Firstly, a piece of CF with size of 1 cm × 3 cm was ultrasonically rinsed in acetone, 3.0 M hydrochloric acid solution, deionized water, as well as anhydrous ethanol for 10 min, consecutively, to eliminate the surface impurity. Then, the washed CF was dried at 60 °C for 12 h under vacuum. Subsequently, 20 ml of aqueous thiourea solution (concentration: 50 mM) was transferred into a Teflon-lined stainless steel autoclave (capacity: 30 mL) containing a piece of cleaned CF, followed by a hydrothermal procedure at 210 °C for 18 h. After cooling to the room temperature naturally, the final product was taken out and cleaned with deionized water and ethanol for each three times, respectively. The obtained CF was uniformly covered with a thin layer of Co_9S_8.

To synthesize nitrogen and phosphorous co-doped Co_9S_8 (N,P-Co_9S_8), the above obtained pristine Co_9S_8 on CF was further annealed in a tube furnace at 300 °C for 60 min under Ar atmosphere (heating rate: 5 C min^{-1}). In the furnace, the mixture of 1 g of $NaH_2PO_2 \cdot H_2O$ and 1 g of $(NH_4)_2HPO_4$, used as

nitrogen and phosphorous source, was placed on the upstream side. Moreover, N,P-Co_9S_8-t (t = 0.5 and 2) was also prepared at annealing temperature of 300 °C for 0.5 and 2 h, respectively. Moreover, nitrogen or phousphorous single doped Co_9S_8, labeled as N-Co_9S_8 or P-Co_9S_8, was further prepared using the same calcination method solely in presence of 1 g of $NaH_2PO_2 \cdot H_2O$ or 1 g of $(NH_4)_2HPO_4$. As a comparison, Co_9S_8-Ar was obtained by annealing pristine Co_9S_8 in absence of nitrogen and phosphorus source.

3. Physical characterization

The phase and crystalline structure of all the synthesized Co_9S_8 materials was performed on Rigaku Ultima IV X-ray diffractometer (XRD) equipped with Cu Kα source (λ = 1.5418 Å). Surface elemental composition and valence state were obtained by K-Alpha Kratos X-ray photoelectron spectrometer (XPS) equipped with a monochromatic X-ray source (Al Kα *hv* = 1486.6 eV). The energy scale of the spectrometer was calibrated with C 1s peak position at 284.8 eV. The Raman spectra were conducted on HORIBA LabRAM HR Evolution with an air-cooled argon ion laser as the exciting source (20 mW, λ = 532 nm). The morphological information was recorded on PHILIPS XL-30ESEM field emission environmental scanning electron microscope (FE-SEM). The transmission electron microscope (TEM), high-resolution (HR-TEM), and the elemental distribution images were obtained on the JEOL JEM-2100 microscope. A contact angle measuring instrument (SINDIN SDC-100s) was used to measure the water contact angle and underwater bubble contact angle at room temperature. The penetration of water droplets and the release of bubbles on the surface of electrode were observed and recorded on a high-speed camera. The volume of water droplet and air bubble was set to be 5 μL.

4. Electrochemical measurements

The electrochemical HER measurements were performed on an electrochemical workstation (CH Instruments, 760E) with a traditional three-electrode configuration in 1.0 M KOH solution. In the typical

cell, the synthesized Co_9S_8-based materials were directly used as the working electrodes, a graphitic carbon rod (diameter: 5 mm) and a Hg/HgO electrode were employed as the counter and reference electrodes, respectively. All the working electrodes were tested with a consistent area of 0.5*0.5 cm^2. All the recorded potentials versus reference electrode were corrected to the potentials with respect to the reversible hydrogen electrode (RHE) based on the calibration experiment. Polarization curves were conducted at a sweep rate of 5 mV s^{-1} after 30 cycles of cyclic voltammetry (CV) activation scanning and recorded with 90 % *iR*-compensation. Tafel plots were determined from the corresponding polarization curves using Tafel equation. Electrochemical impedance spectroscopies (EIS) were carried out at an overpotential of 160 mV with amplitude voltage of 10 mV from 0.1 to 10^5 Hz and all of them were fitted with the Randles equivalent circuit. The double-layer capacitance (C_{dl}) values were calculated through different CV scans in the non-Faradic potential from 0.045 to 0.145 V (*vs.* RHE) with variable scan rates from 40 to 120 mV s^{-1}. A linear curve was obtained by plotting capacitive current (J_{anodic}-$J_{cathodic}$) versus scan rate at 0.095 V (*vs.* RHE), where half of the slope was supposed to be C_{dl} value. The electrochemical surface area (ECSA) was then estimated by the equation of ESCA ≈ C_{dl} / C_s, where C_s is the capacitance of an atomically smooth planar electrocatalyst surface per unit area under identical media conditions and is reported to be around 0.04 mF cm^{-2} in 1.0 M KOH electrolyte. To determine the long-term stability, chronopotentiometry curve was acquired over N,P-Co_9S_8 electrode at a large static current density of 100 mA cm^{-2} for 10 h in 1.0 KOH solution, after which polarization curves and Tafel slops were further obtained. The Faradaic efficiency (FE) in HER was conducted at potential of -0.15 V *vs.* RHE in a period of 35 min. Its value can be defined as the ratio of experimentally collected hydrogen quantity to the theoretically expected amount during this period.

Similarly, the linear sweep voltammetry (LSV) curves toward OER over Co_9S_8 and N,P-Co_9S_8 electrodes in 1.0 M KOH electrolyte were also acquired with a sweep rate of 5 mV s^{-1}. The corresponding Tafel slopes were obtained from LSV curves. The durability was evaluated with chronopotentiometry

method at the constant large anodic current density of 100 mA cm^{-2} for 24 h. The overall water splitting performance was conducted at different temperature (25, 35, 50, 65, 90 °C) in a standard two-electrode electrolyzer using N,P-Co_9S_8 as both cathode and anode in 1.0 M KOH solution. LSV curves were recorded with the scan rate of 5 mV s^{-1} after 30 cycles of CV activation process. Furthermore, the stability test of electrolyzer was carried out at 65 °C with the current density of 100 mA cm^{-2} for 12 h.

Additional results

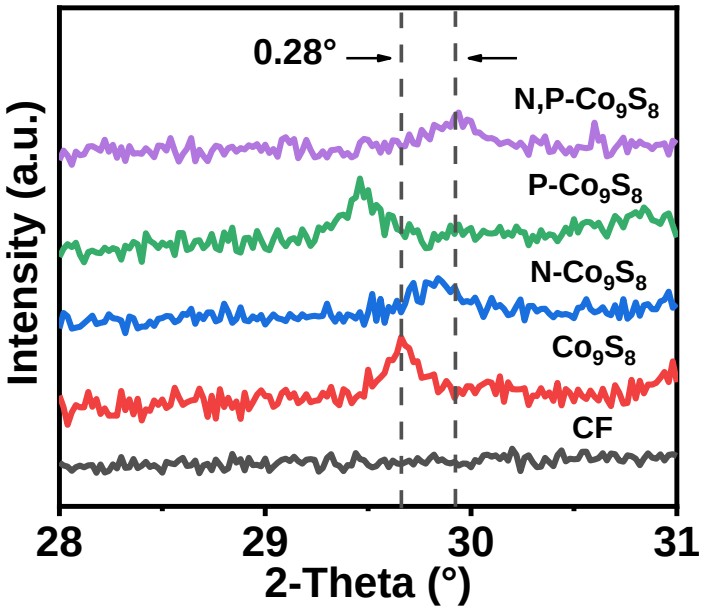

Figure S1. The enlarged XRD patterns of CF, pristine Co_9S_8, and anions doped Co_9S_8 in the 2θ range of 28-31 °.

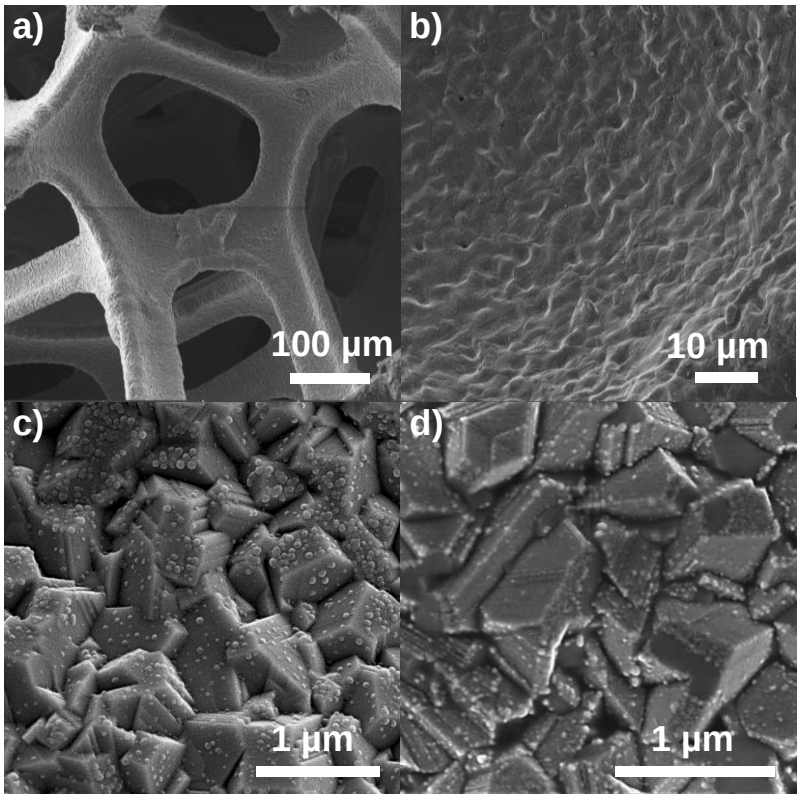

Figure S2. SEM images of a, b) Cobalt Foam, c) N-Co_9S_8 and d) P-Co_9S_8.

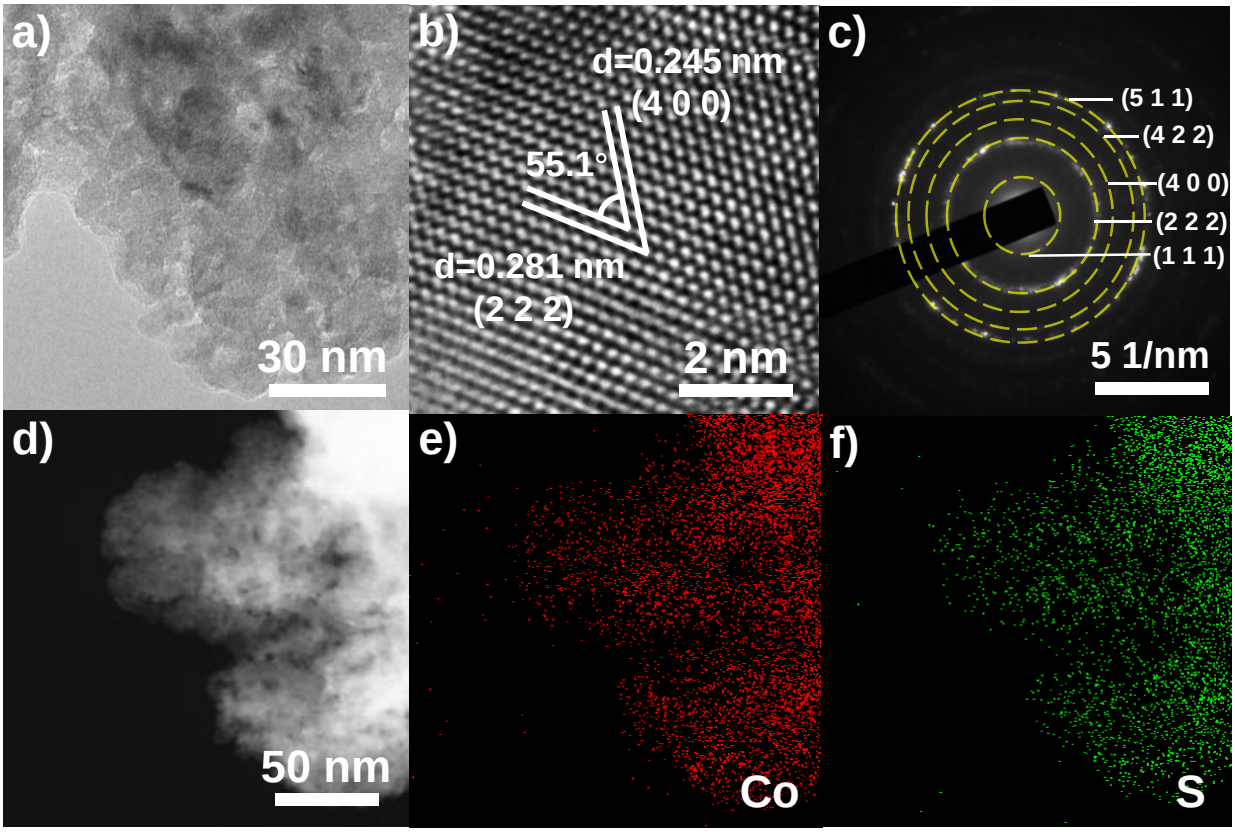

Figure S3. a) TEM, b) HR-TEM images and c) the corresponding SAED pattern of pristine Co_9S_8. d) HAADF-STEM image, e, f) the elemental distribution mapping images of Co and S, respectively.

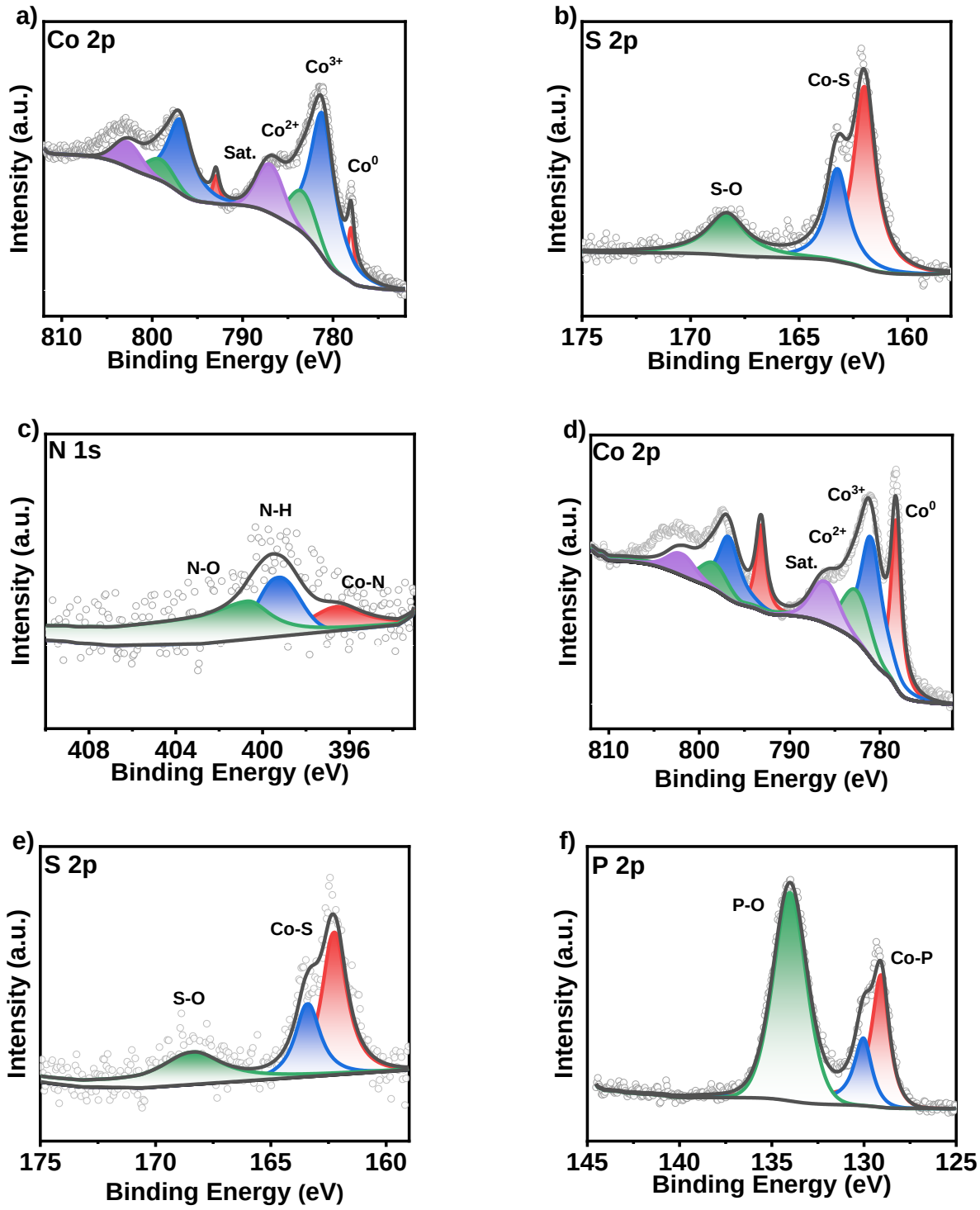

Figure S4. High-resolution XPS spectra for a) Co 2p, b) S 2p, c) N 1s of N-Co_9S_8, and d) Co 2p, e) S 2p, f) P 2p of P-Co_9S_8.

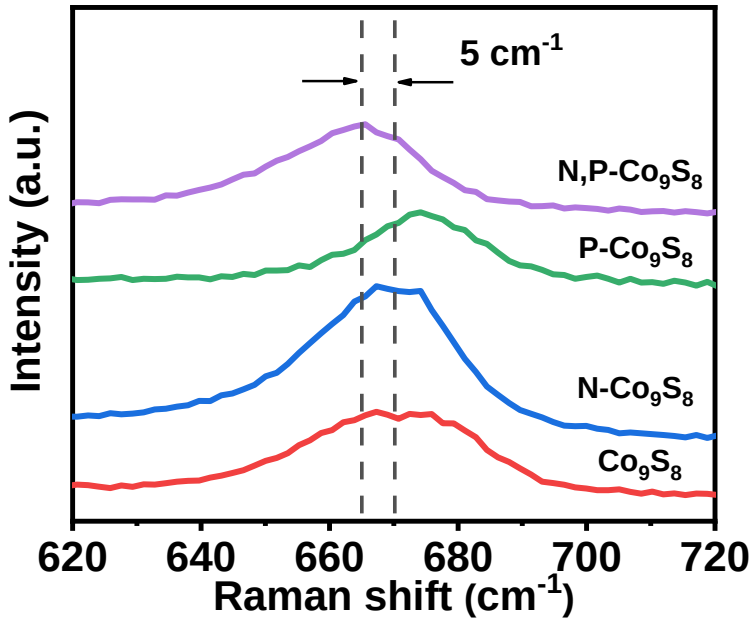

Figure S5. The enlarged Raman spectra of pristine Co_9S_8 and the anions doped one in the range of 620-720 cm^{-1}.

.

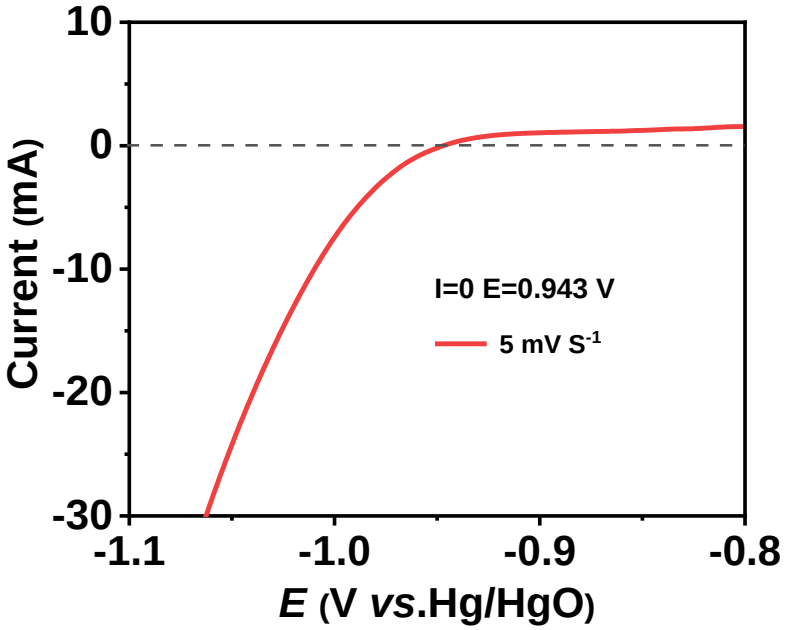

Figure S6. The result of RHE calibration experiment.

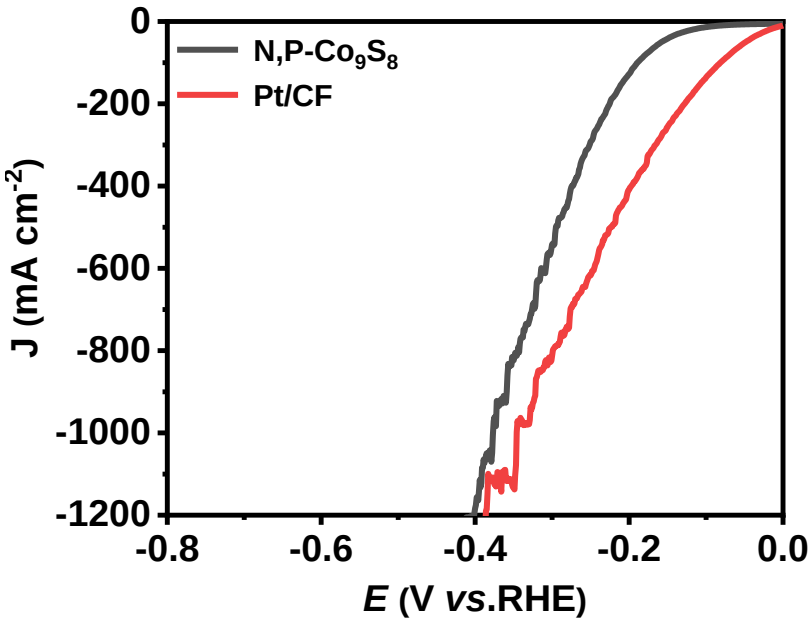

Figure S7. LSV curves toward HER over N,P-Co_9S_8 and commercial Pt/C (20 wt. %) on CF in 1.0 M KOH electrolyte.

Table S1. The electrochemical activity in alkaline toward HER over N,P-Co_9S_8 compared with some currently reported cobalt-based HER electrocatalysts.

Sample	*Conc.*(M,KOH)	$\eta_{j=10\ mA\ cm^{-2}}$ (mV)	Reference
N,P-Co_9S_8	**1.0**	**80**	**This work**
Co-OSP-0.2	**1.0**	**132.7**	**S1**
Co_9S_8-MoS_2/NF	**1.0**	**110**	**S2**
$Cu_{1.96}S$/ Co_9S_8	**1.0**	**99**	**S3**
Co/CoO@NC@CC	**1.0**	**152**	**S4**
Co_9S_8/Ni_3S_2	**1.0**	**128**	**S5**
$ZnCo_2S_4$/$CoZn_{13}$	**1.0**	**98.2**	**S6**
Co@CoFe-NBs	**1.0**	**104**	**S7**
Fe-CoP/$Ni(OH)_2$	**1.0**	**91**	**S8**
CC/MOF-$CoSe_2$@$MoSe_2$	**1.0**	**109.87**	**S9**
Fe–Co–Ni MOF	**1.0**	**116**	**S10**
Co-Mo_2C-CN_x-2	**1.0**	**92**	**S11**
Co-$Co_{0.85}$-Ce	**1.0**	**97**	**S12**

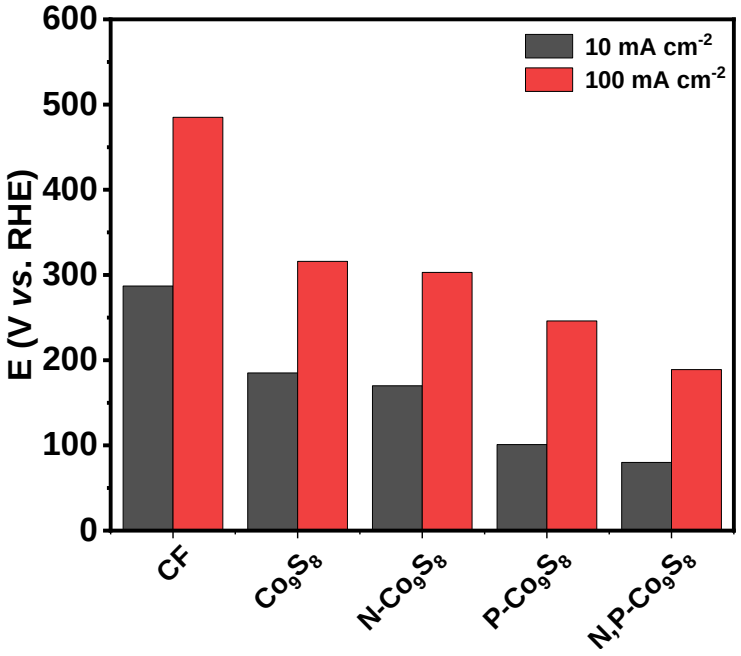

Figure S8. The corresponding histograms of overpotentials at j = 10 and 100 mA cm^{-2} for CF and Co_9S_8-based materials.

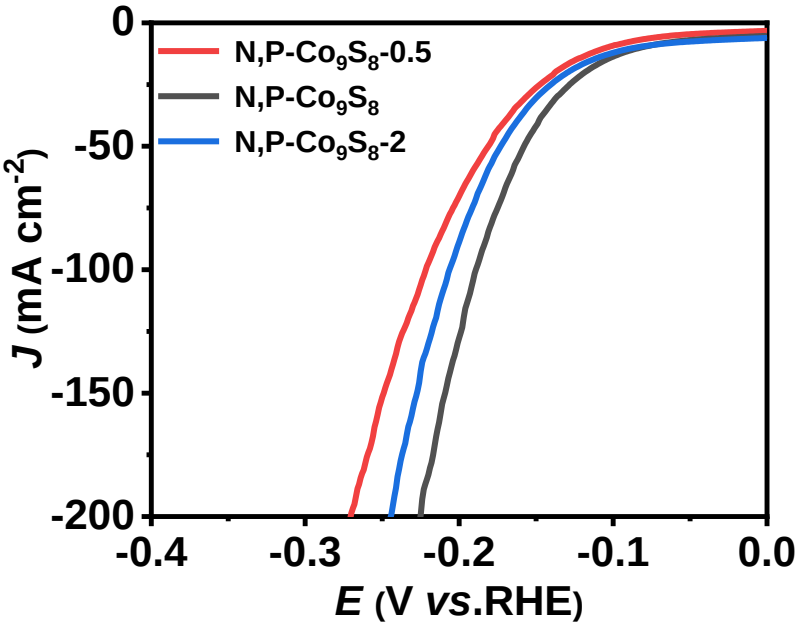

Figure S9. LSV curves toward HER over N,P-Co_9S_8, N,P-Co_9S_8-0.5 and N,P-Co_9S_8-2 in 1.0 M KOH electrolyte.

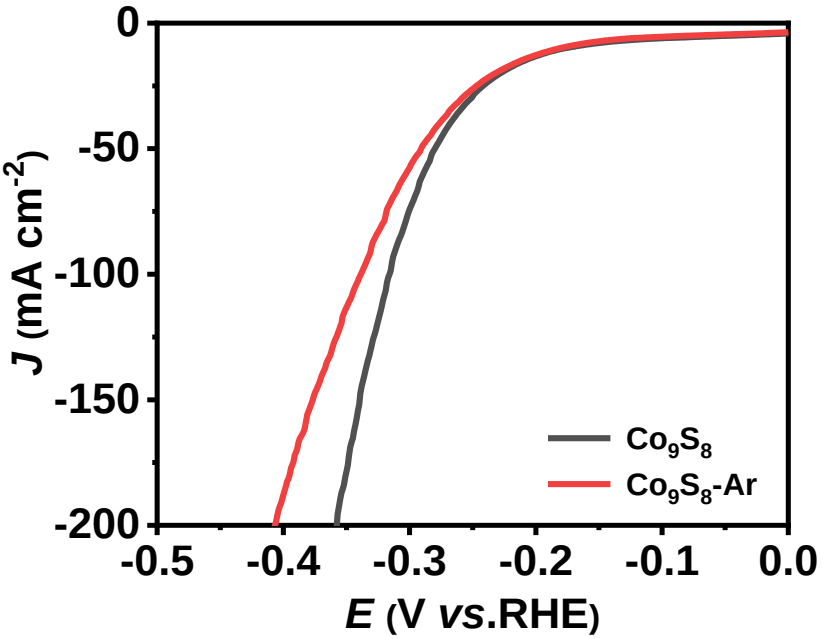

Figure S10. LSV curves toward HER in 1.0 M KOH electrolyte over pristine Co_9S_8 and Co_9S_8 after heat treatment in absence of nitrogen and phosphorous source (Co_9S_8-Ar).

Table S2. Summary of electrochemical performance toward HER in 1.0 M KOH electrolyte for CF and Co_9S_8-based materials.

Sample	$\eta_{j=10\ mA\ cm^{-2}}$ (mV)	$\eta_{j=100\ mA\ cm^{-2}}$ (mV)	Tafel slope (mV dec^{-1})	R_{ct} (Ω)	C_{dl} (mF cm^{-2})	ECSA (cm^2)
CF	287	485	200	421.4	10.3	257.5
Co_9S_8	185	316	168	36.1	40.2	1005
N- Co_9S_8	170	303	163	20.9	42.1	1052.5
P- Co_9S_8	101	246	157	19.5	44.7	1117.5
N,P-Co_9S_8	80	189	104	9.32	50.7	1267.5

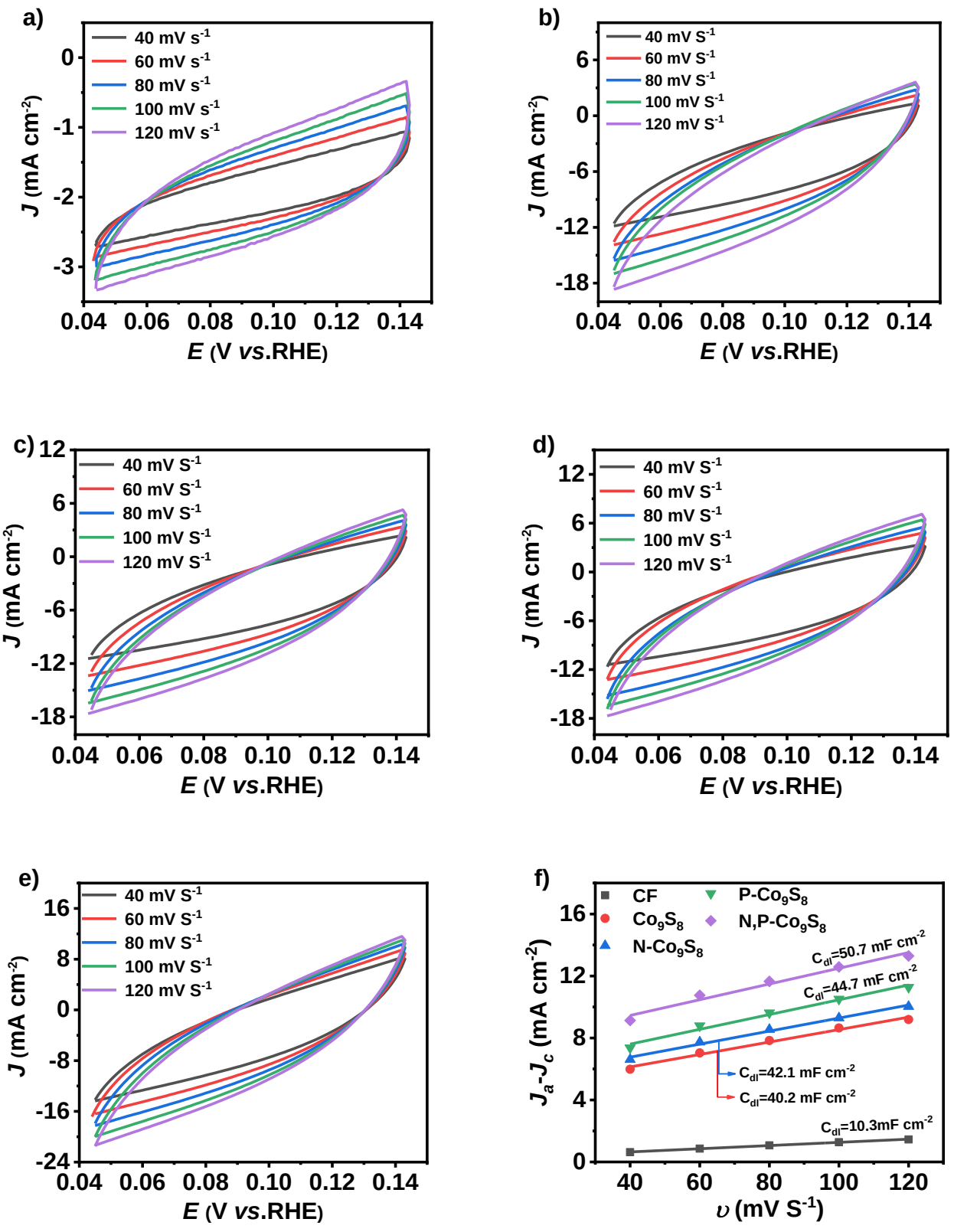

Figure S11. CV curves for ECSA measurements in 1.0 M KOH solution in the non-Faradaic window of 0.04 to 0.14 V with different scan sweeps (*i.e.* 40, 60, 80, 100,120 mV s^{-1}) over a) CF, b) Co_9S_8, c) N-Co_9S_8, d) P-Co_9S_8, and e) N,P-Co_9S_8 electrodes, respectively. f) Capacitive current densities obtained from a-e) at the potential of 0.09 V as function of scan rates.

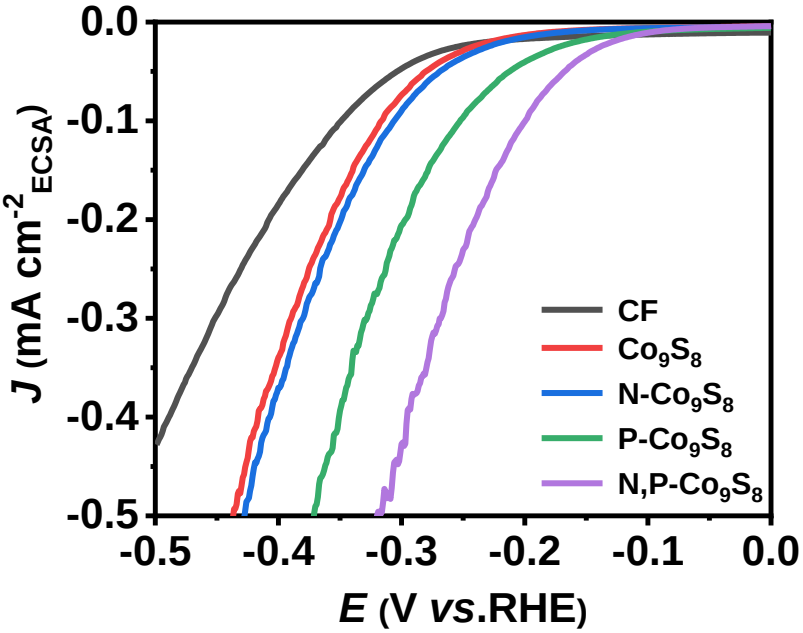

Figure S12. LSV curves with the current density normalized by ECSA over CF and Co_9S_8-based electrodes in 1.0 M KOH solution.

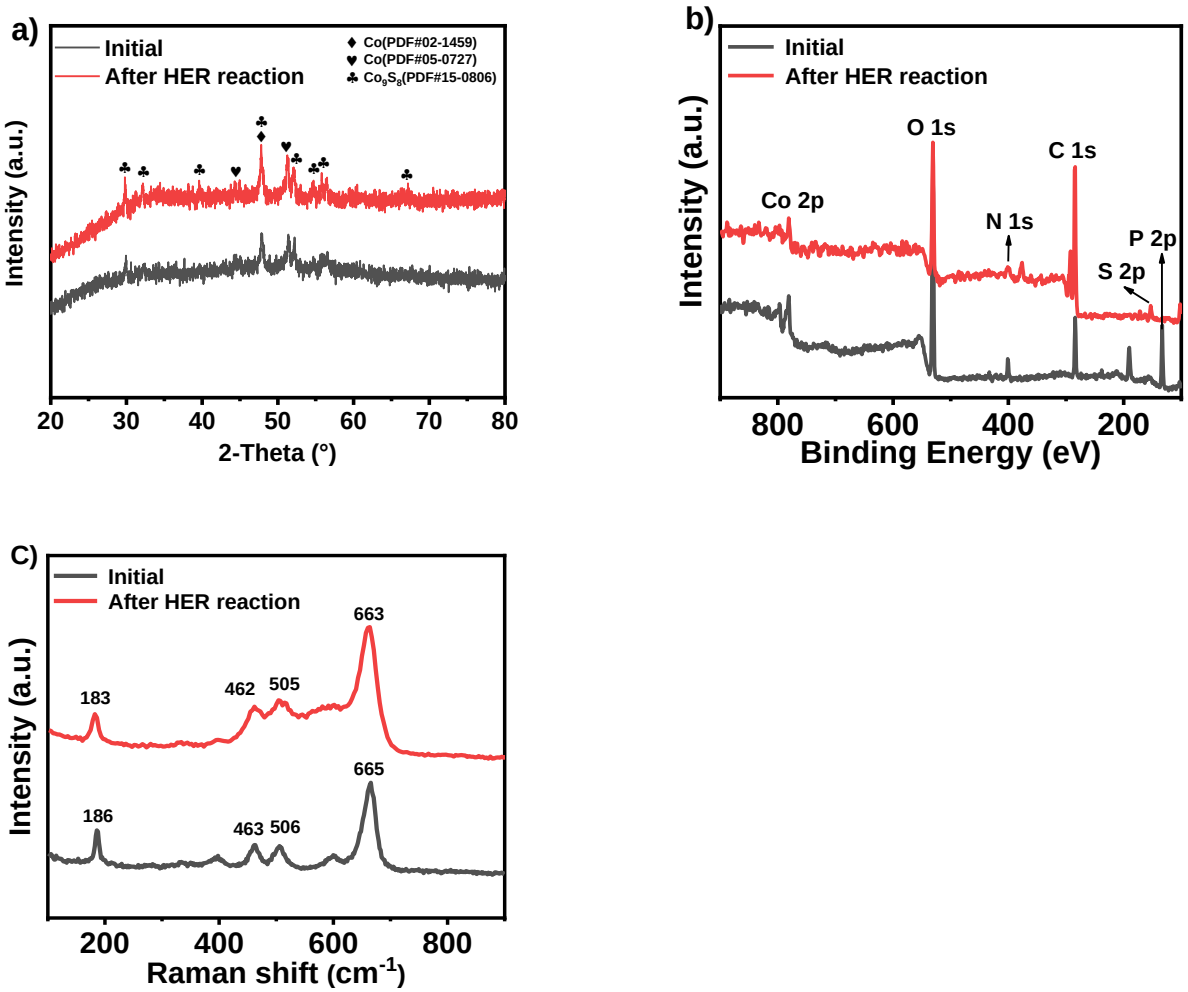

Figure S13. a) XRD patterns, b) XPS survey spectra and c) Raman spectra of N,P-Co_9S_8 before and after long-term stability test at large current density toward HER.

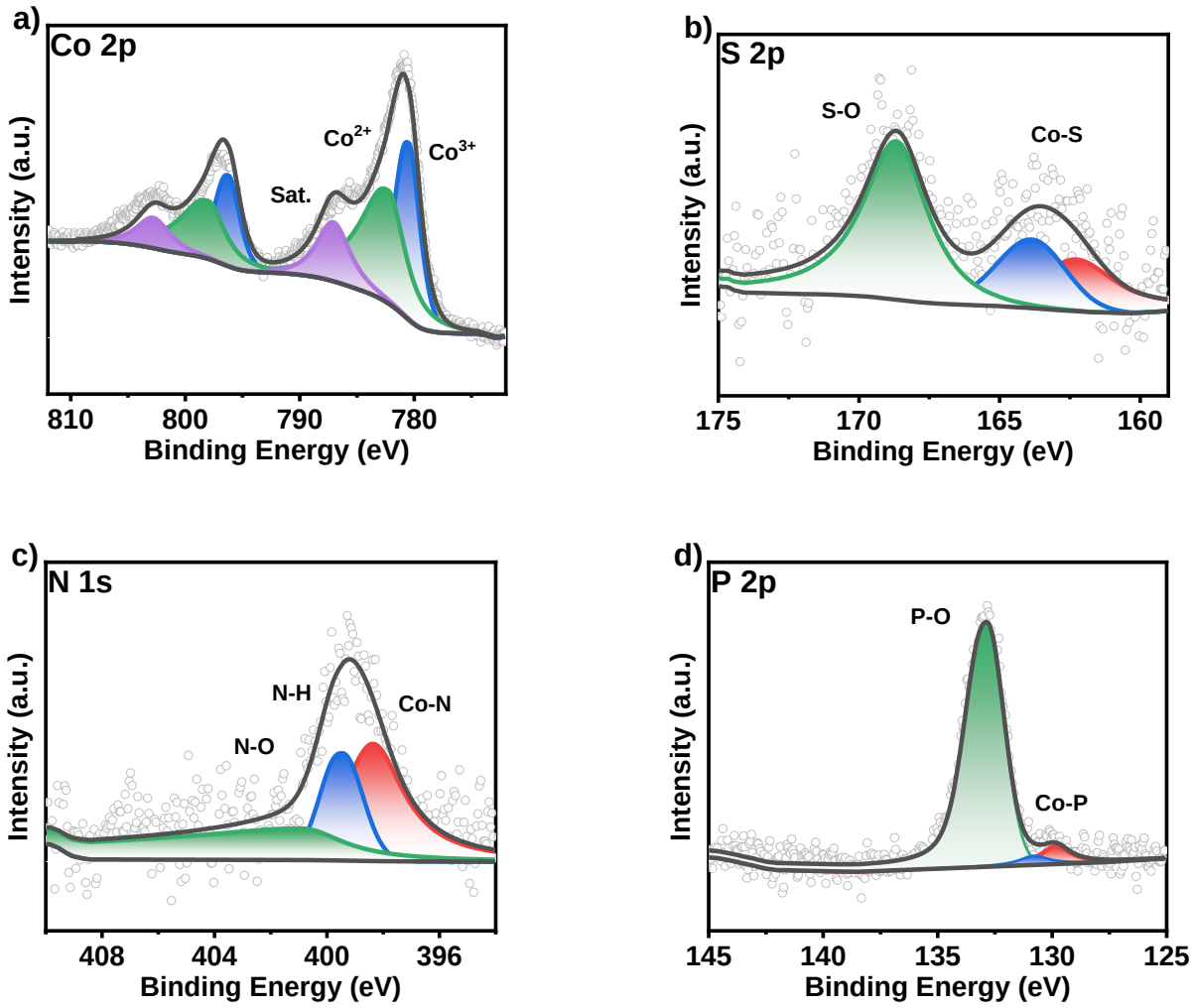

Figure S14. High-resolution XPS spectra for a) Co, b) S, c) N, and d) P of N,P-Co_9S_8 after stability test, respectively.

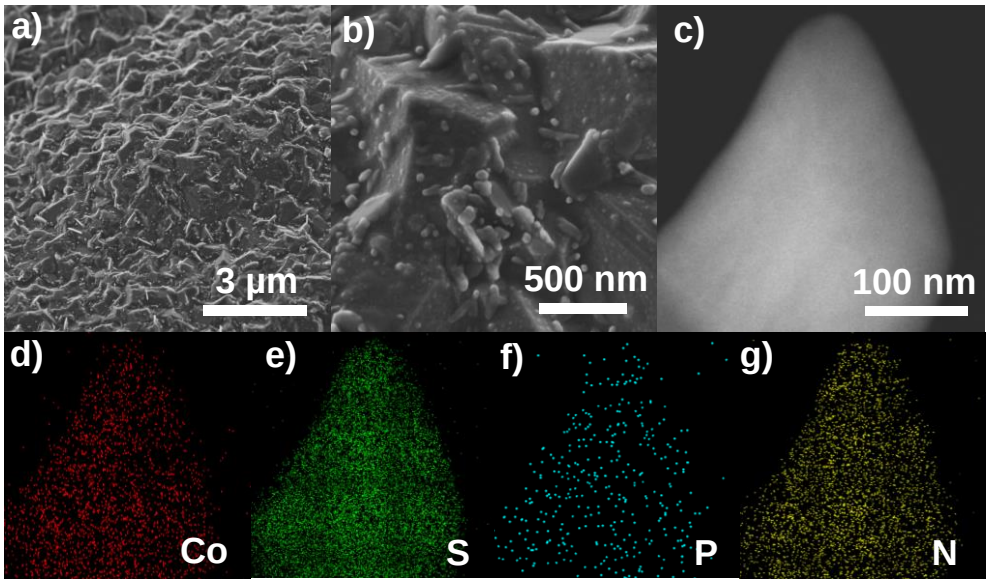

Figure S15. Morphological and elemental information of N,P-Co_9S_8 electrode after long-term stability test at a large current density toward HER. a) and b) SEM images, c) HAADF-STEM image, d-g) the elemental distribution mapping images of Co, S, P, and N, respectively.

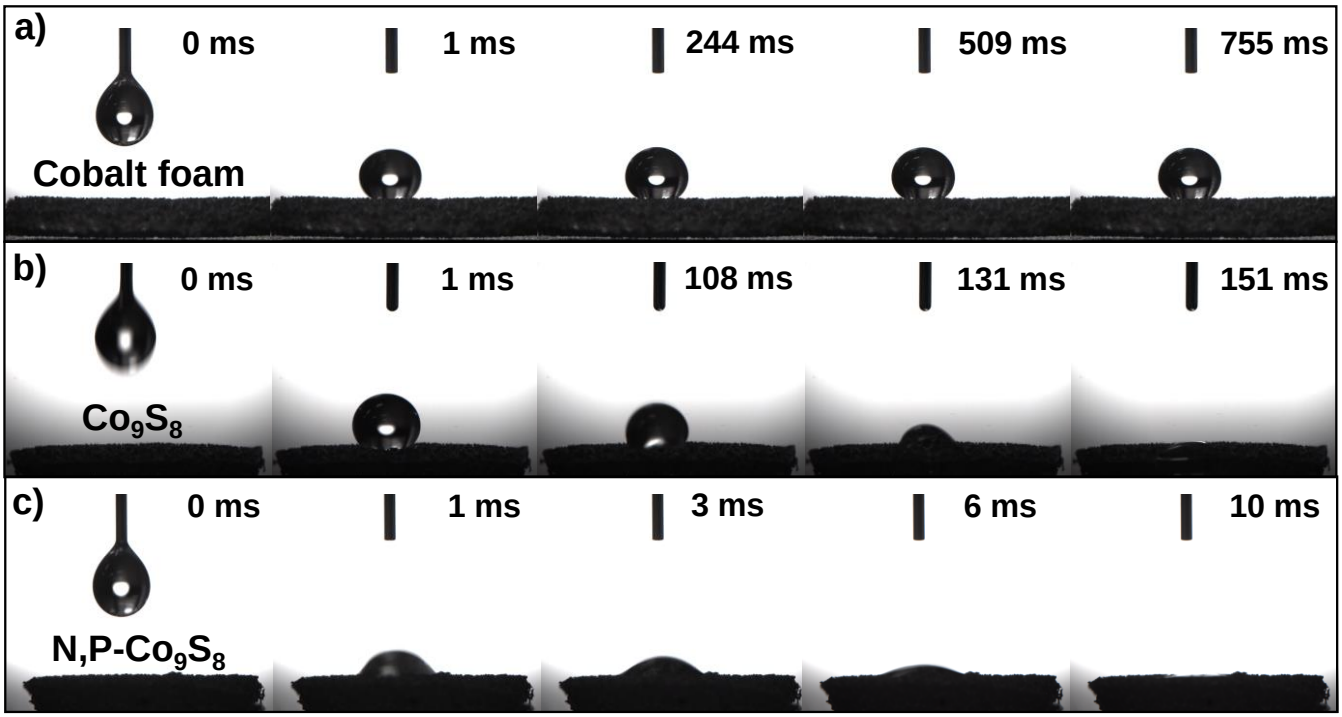

Figure S16. Water contact angle measurement of a) CF, b) Co_9S_8, c) N,P-Co_9S_8.

Table S3. The electrochemical activity in alkaline toward OER over N,P-Co_9S_8 compared with some currently reported cobalt-based OER electrocatalysts.

Sample	*Conc.*(M,KOH)	$\eta_{j=10\ mA\ cm^{-2}}$ (mV)	$\eta_{j=100\ mA\ cm^{-2}}$ (mV)	Reference
N,P-Co_9S_8	1.0	240(50 mA cm^{-2})	320	This work
Co_3O_4@CoP	1.0	238	370	S13
N-CoO	1.0	319	410	S14
CoS_2/MoS_2@CC	1.0	274	340	S15
Co_3O_4-250	1.0	275	360	S16
CoO@S-CoTe	1.0	246	362	S17
Co_3O_4/$CoMoO_4$-0.1-FO	1.0	217	342	S18
NCP/G NSs	1.0	/	400	S19
S:CoP@NF	1.0	300	360	S20
Co-Mo-P/CoNWs	1.0	/	320	S21
Co_9S_8@Co_3O_4/NF	1.0	/	331	S22

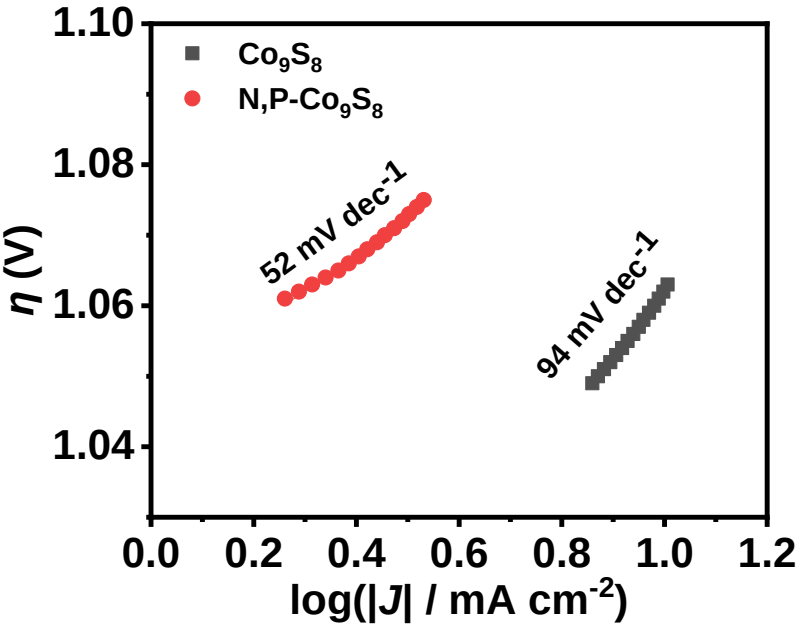

Figure S17. Tafel slopes of Co_9S_8 and N,P-Co_9S_8.

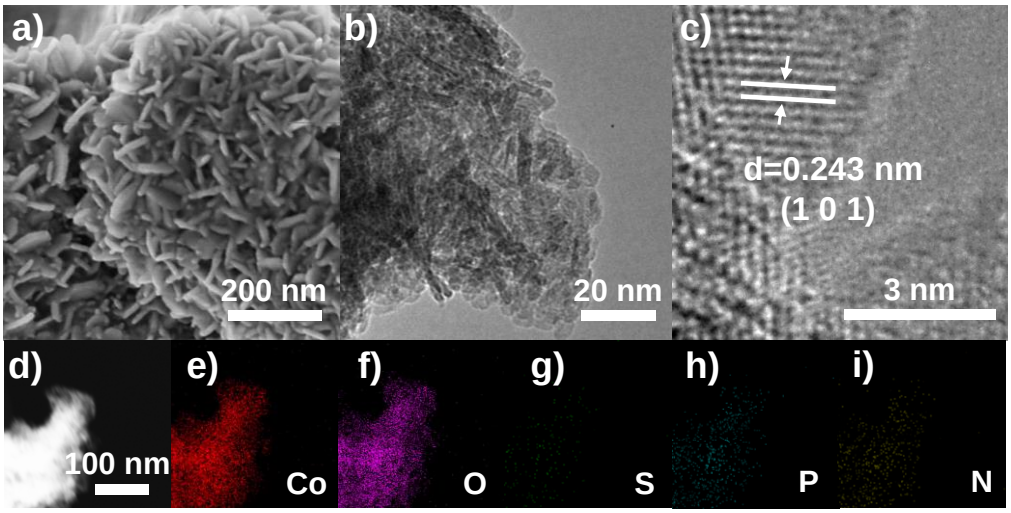

Figure S18. Morphological and elemental information of N,P-Co_9S_8 electrode after long-term stability test at a large current density toward OER. a) SEM, b) TEM and c) HR-TEM images, d) HAADF-STEM image, e-i) the elemental distribution mapping images of Co, O, S, P, and N, respectively.

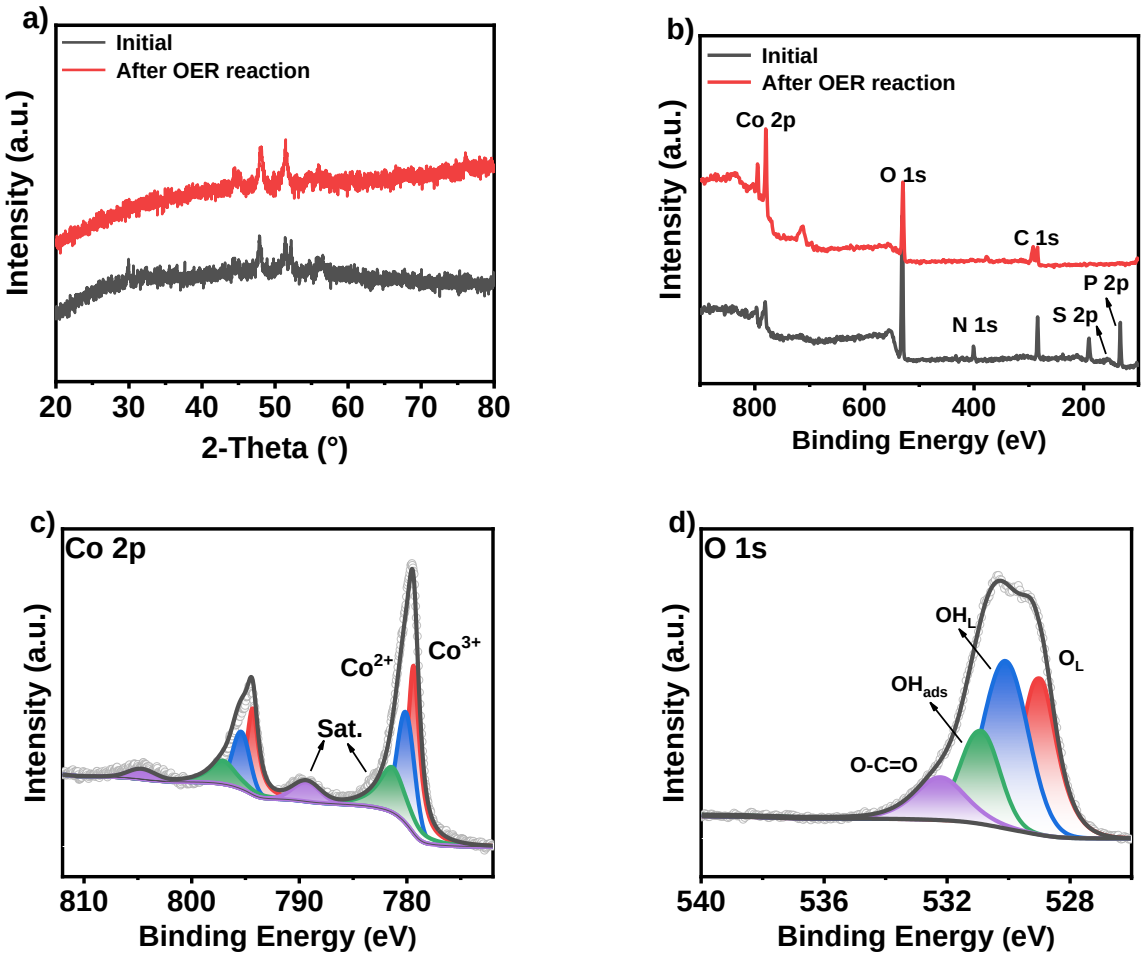

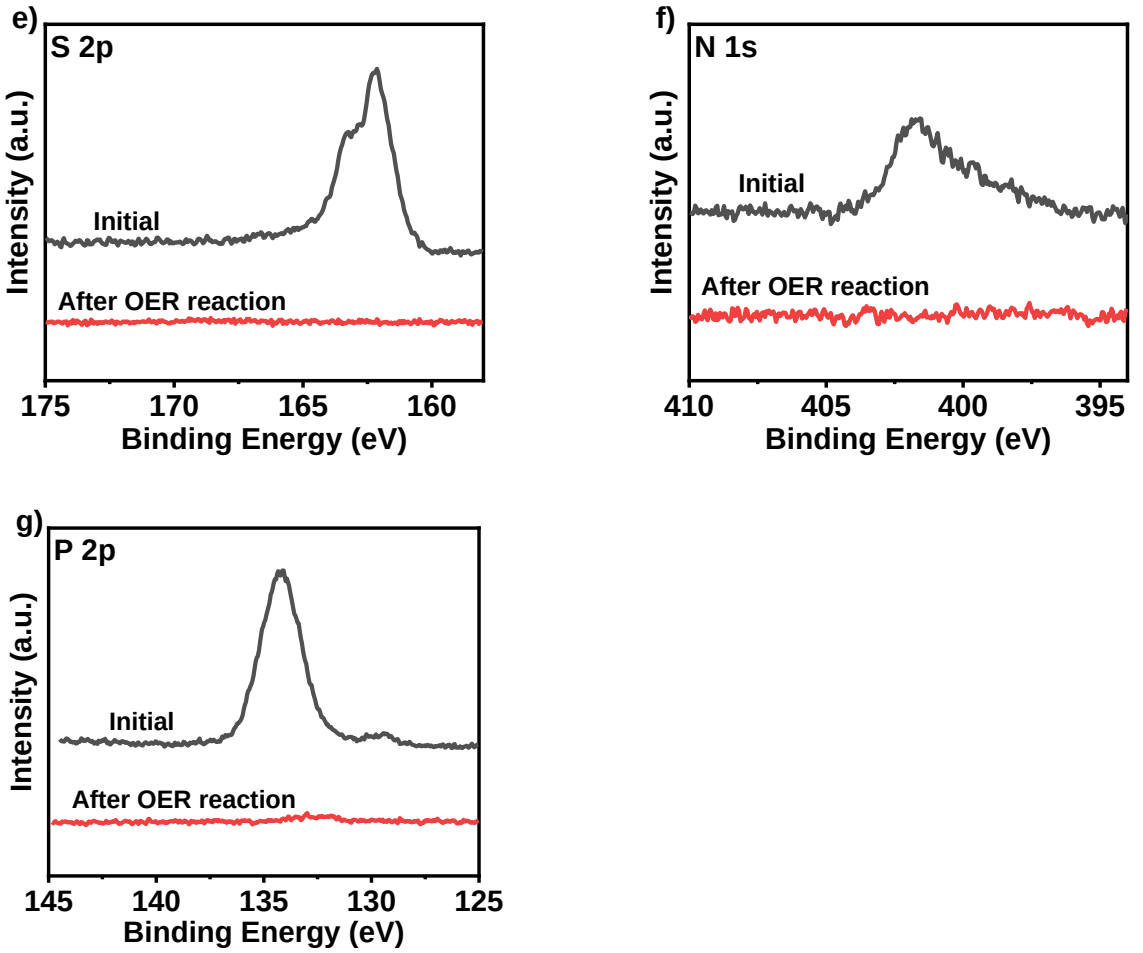

Figure S19. a) XRD patterns, b) XPS survey spectra of N,P-Co_9S_8 before and after long-term stability test at large current density toward OER. High-resolution XPS spectra for c) Co, d) O, e) S, f) N and g) P of N,P-Co_9S_8 after stability test, respectively.

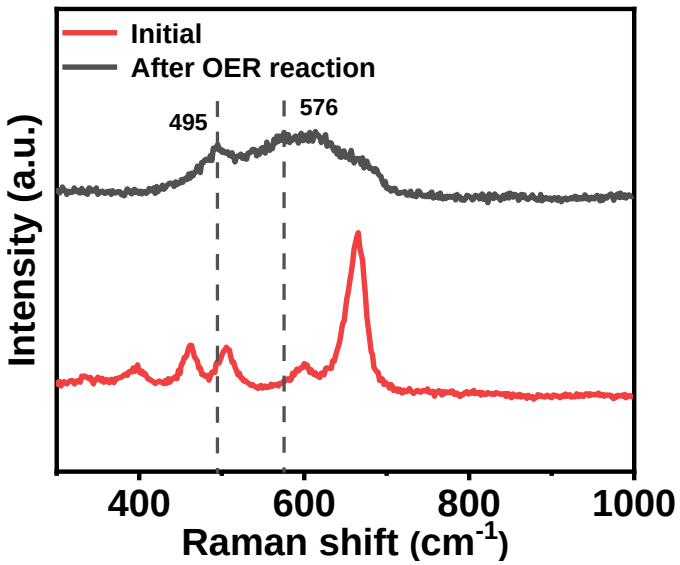

Figure S20. Raman spectra of N,P-Co_9S_8 after OER.

Reference

S1. B. Chong, M. Xia, Y. Lv, H. Li, X. Yan, B. Lin, G. Yang, Hierarchical phosphorus-oxygen incorporated cobalt sulfide hollow micro/nano-reactor for highly-efficient electrocatalytic overall water splitting, *Chem. Eng. J*., 2023, **465**, 142853.

S2. M. Kim, M.A.R. Anjum, M. Choi, H.Y. Jeong, S.H. Choi, N. Park, J.S. Lee, Covalent 0D–2D Heterostructuring of Co_9S_8–MoS_2 for Enhanced Hydrogen Evolution in All pH Electrolytes, *Adv. Funct. Mater*., 2020, **30**, 2002536.

S3. Y. Xiao, Y. Shen, D. Su, S. Zhang, J. Yang, D. Yan, S. Fang, X. Wang, Engineering $Cu_{1.96}S/Co_9S_8$ with sulfur vacancy and heterostructure as an efficient bifunctional electrocatalyst for water splitting, *J. mater. sci. technol*., 2023, **154**, 1-8.

S4. K. Dai, N. Zhang, L. Zhang, L. Yin, Y. Zhao, B. Zhang, Self-supported Co/CoO anchored on N-doped carbon composite as bifunctional electrocatalyst for efficient overall water splitting, *Chem. Eng. J*., 2021, **414**, 128804.

S5. F. Du, L. Shi, Y. Zhang, T. Li, J. Wang, G. Wen, A. Alsaedi, T. Hayat, Y. Zhou, Z. Zou, Foam–like Co_9S_8/Ni_3S_2 heterostructure nanowire arrays for efficient bifunctional overall water–splitting, *Appl. Catal. B*, 2019, **253**, 246-252.

S6. D. Zhao, M. Dai, H. Liu, Z. Duan, X. Tan, X. Wu, Bifunctional $ZnCo_2S_4@CoZn_{13}$ hybrid electrocatalysts for high efficient overall water splitting, *J. Energy Chem*., 2022, **69**, 292-300.

S7. Y. Zhao, N. Dongfang, C.A. Triana, C. Huang, R. Erni, W. Wan, J. Li, D. Stoian, L. Pan, P. Zhang, J. Lan, M. Iannuzzi, G.R. Patzke, Dynamics and control of active sites in hierarchically nanostructured cobalt phosphide/chalcogenide-based electrocatalysts for water splitting, *Energy Environ. Sci*., 2022, **15**, 727-739.

S8. X. Yu, J. Zhao, M. Johnsson, Interfacial Engineering of Nickel Hydroxide on Cobalt Phosphide for Alkaline Water Electrocatalysis, *Adv. Funct. Mater*., 2021, **31**, 2101578.

S9. S.J. Patil, N.R. Chodankar, S.-K. Hwang, P.A. Shinde, G. Seeta Rama Raju, K. Shanmugam Ranjith,

Y.S. Huh, Y.-K. Han, Co-metal–organic framework derived $CoSe_2$@$MoSe_2$ core–shell structure on carbon cloth as an efficient bifunctional catalyst for overall water splitting, *Chem. Eng. J.*, 2022, **429**, 132379.

S10. F. Shahbazi Farahani, M.S. Rahmanifar, A. Noori, M.F. El-Kady, N. Hassani, M. Neek-Amal, R.B. Kaner, M.F. Mousavi, Trilayer Metal-Organic Frameworks as Multifunctional Electrocatalysts for Energy Conversion and Storage Applications, *J. Am. Chem. Soc*., 2022, **144**, 3411-3428.

S11. P. Zhang, Y. Liu, T. Liang, E.H. Ang, X. Zhang, F. Ma, Z. Dai, Nitrogen-doped carbon wrapped Co-Mo_2C dual Mott–Schottky nanosheets with large porosity for efficient water electrolysis, *Appl. Catal. B*, 2021, **284**, 119738.

S12. J. Yu, W. Yu, Y. Wang, X. Li, R. Liu, X. Zhang, H. Liu, W. Zhou, Capture and recycling of toxic selenite anions by cobalt-based metal-organic-frameworks for electrocatalytic overall water splitting, *Chem. Eng. J*., 2022, **433**, 134553.

S13. J. Zhou, Y. Dou, A. Zhou, R.-M. Guo, M.-J. Zhao, J.-R. Li, MOF Template-Directed Fabrication of Hierarchically Structured Electrocatalysts for Efficient Oxygen Evolution Reaction, *Adv. Energy Mater*., 2017, **7**, 1602643.

S14. K. Zhang, X. Xia, S. Deng, D. Xie, Y. Lu, Y. Wang, J. Wu, X. Wang, J. Tu, N-doped CoO nanowire arrays as efficient electrocatalysts for oxygen evolution reaction, *J. Energy Chem*., 2019, **37**, 13-17.

S15. G. Zhou, X. Wu, M. Zhao, H. Pang, L. Xu, J. Yang, Y. Tang, Interfacial Engineering-Triggered Bifunctionality of CoS_2/MoS_2 Nanocubes/Nanosheet Arrays for High-Efficiency Overall Water Splitting, *ChemSusChem*, 2021, **14,** 699-708.

S16. G. Cheng, T. Kou, J. Zhang, C. Si, H. Gao, Z. Zhang, O_2^{2-} /O^- functionalized oxygen-deficient Co_3O_4 nanorods as high performance supercapacitor electrodes and electrocatalysts towards water splitting, *Nano Energy*, 2017, **38**, 155-166.

S17. X. Wang, Z. Mao, X. Mao, X. Hu, F. Gao, M. Gao, Q.L. Wu, X. Lyu, A. Du, X. Xu, Y. Jia, L. Wang,

Dual Integrating Oxygen and Sulphur on Surface of CoTe Nanorods Triggers Enhanced Oxygen Evolution Reaction, *Adv. Sci*., 2023, **10**, e2206204.

S18. L. Xia, L. Bo, W. Shi, Y. Zhang, Y. Shen, X. Ji, X. Guan, Y. Wang, J. Tong, Defect and interface engineering of templated synthesis of hollow porous $Co_3O_4/CoMoO_4$ with highly enhanced electrocatalytic activity for oxygen evolution reaction, *Chem. Eng. J*., 2023, **452**, 139250.

S19. J. Tian, J. Chen, J. Liu, Q. Tian, P. Chen, Graphene quantum dot engineered nickel-cobalt phosphide as highly efficient bifunctional catalyst for overall water splitting, *Nano Energy*, 2018, **48**, 284-291.

S20. M.A.R. Anjum, M.S. Okyay, M. Kim, M.H. Lee, N. Park, J.S. Lee, Bifunctional sulfur-doped cobalt phosphide electrocatalyst outperforms all-noble-metal electrocatalysts in alkaline electrolyzer for overall water splitting, *Nano Energy*, 2018, **53**, 286-295.

S21. V.H. Hoa, D.T. Tran, D.C. Nguyen, D.H. Kim, N.H. Kim, J.H. Lee, Molybdenum and Phosphorous Dual Doping in Cobalt Monolayer Interfacial Assembled Cobalt Nanowires for Efficient Overall Water Splitting, *Adv. Funct. Mater*., 2020, **30**, 2002533.

S22. X. Wang, Y. He, X. Han, J. Zhao, L. Li, J. Zhang, C. Zhong, Y. Deng, W. Hu, Engineering cobalt sulfide/oxide heterostructure with atomically mixed interfaces for synergistic electrocatalytic water splitting, *Nano Res*., 2021, **15**, 1246-1253.